

**Zig-zag wall lattice in a nematic liquid crystal with an in-plane switching configuration**I. Andrade-Silva,<sup>\*</sup> M. G. Clerc,<sup>†</sup> and V. Odent<sup>‡</sup>*Departamento de Física, Facultad de Ciencias Físicas y Matemáticas, Universidad de Chile, Casilla 487-3, Santiago, Chile*

(Received 22 April 2014; published 26 August 2014)

Liquid crystals displays with tailoring electrodes exhibit complex spatiotemporal dynamics when a large voltage is applied. We report experimental observations of the appearance of a programmable zig-zag lattice using an in-plane-switching cell filled with a nematic liquid crystal. Applying a small voltage to a wide range of frequencies, the system exhibits an Ising wall lattice. Increasing the voltage, this lattice presents a spatial instability generating an undulating wall lattice, and to higher voltages it becomes zig-zag type. Experimentally, we characterize the bifurcations and phase diagram of the wall lattice. Theoretically, we develop, from first principles, a descriptive model. This model has a good qualitative agreement with experimental observations.

DOI: [10.1103/PhysRevE.90.022504](https://doi.org/10.1103/PhysRevE.90.022504)

PACS number(s): 61.30.Gd, 47.20.Ma, 47.20.Ky

**I. INTRODUCTION**

Liquid crystals are made of anisotropic-shaped organic molecules [1–5]. This results in a strong anisotropy of all their physical properties, especially optical features [2–5]. In the nematic phase, the lowest-energy configuration is reached when all the rodlike molecules are aligned along a mean direction represented by a unit vector  $\mathbf{n}$  called the director. Since this vector shows only a direction and not a particular sense, any description must include the symmetry  $\mathbf{n} \leftrightarrow -\mathbf{n}$ . This direction can be specified either by applying an external field, like an electric or magnetic one, or by imposing some particular boundary conditions—anchoring conditions—at the edges of the confined sample. When two of these constraints are competing, the long-range orientational order may be partially destroyed. Thus, orientational deformations then appear in the sample. These deformations are theoretically described by a vector field  $\mathbf{n}(\vec{r}, t)$  which points out the averaged orientation of the molecules in the fluid particle located in  $\vec{r}$  and at time  $t$ . This phenomenon actually occurs when one tries to lead the reorientation of the molecules, using an external field, in an anchored layer of nematic liquid crystal. For a field magnitude sufficiently high, the initial alignment, due to the anchoring, is suppressed in the bulk. This phenomenon is usually named the Fréedericksz transition [6]. Due to the twofold degeneracy of the bifurcated state, domains of opposite orientations may be created [7]. The interface between two of these domains is called the *Ising wall* in the homeotropic geometry of the Fréedericksz transition [8], which corresponds to the equivalent of magnetic Ising walls in liquid crystals [9]. In this configuration the molecules are anchored perpendicularly to the boundary glass plates. Thus the Ising wall is a topological defect of the Fréedericksz bifurcation [10–13]. An Ising wall corresponds to an interface separating two symmetric equilibria. These walls, subjected to electric and magnetic fields, can exhibit a zig-zag instability [13–15]. This type of instability is a universal phenomenon, which is observed in various

physical contexts such as in microwrinkle grooves [16], gas discharge systems [17], crystals growth [18], rifts in the spreading wax layer [19], the chevron layer structure of smectic liquid crystals [20], and nematic liquid crystal samples subjected to a temperature gradient [21] or a confinement configuration [22].

The liquid crystals are ubiquitous in our daily lives, due to the adjustability of the molecule orientation, with several applications [23,24], in particular, visual display technology [25,26]. One of these applications is the *liquid crystal display*, with, more specifically, the *in-plane-switching* technology [27], where the electrodes can be designed, by use of deposition processes, with different shapes on a single substrate. This allows us to apply tension in the transverse and vertical directions. Figure 1 shows the typical in-plane-switching configuration. This type of electrode configuration was developed for screen application. The electro-optical characteristics of these types of cells, such as optical transmittance, are well explained by a one-dimensional model [28,29]. When one applies a voltage and surpasses a certain critical value, one expects that the molecules self-organize [30–33] through the creation of different domains separated by walls. Increasing the tension, one expects a complex spatiotemporal walls dynamic.

The aim of this article is to evidence the observation of a programmable zig-zag lattice in a nematic liquid crystal inserted in an in-plane-switching cell. Applying a small voltage in a wide range of frequencies, the system exhibits an Ising wall lattice. Increasing the voltage this lattice presents a spatial supercritical instability generating an undulating lattice, and at higher voltages it becomes a zig-zag lattice. Experimentally, we characterize the bifurcations and phase diagram of the wall lattice. Theoretically, we develop, from first principles, a model to describe the walls dynamical behavior which is described by a nonlinear diffusion equation with a dissipative term. This model has a good qualitative agreement with experimental observations.

The manuscript is organized as follows. In Sec. II, first, is presented the experimental setup of this study. Subsequently, the wall lattice and their respective instabilities are characterized. The theoretical description of the wall lattice is presented in Sec. III. Our conclusions and remarks are left for the final section.

<sup>\*</sup> [iandrade@ing.uchile.cl](mailto:iandrade@ing.uchile.cl)<sup>†</sup> [marcel@dfi.uchile.cl](mailto:marcel@dfi.uchile.cl)<sup>‡</sup> [vodent@ing.uchile.cl](mailto:vodent@ing.uchile.cl)

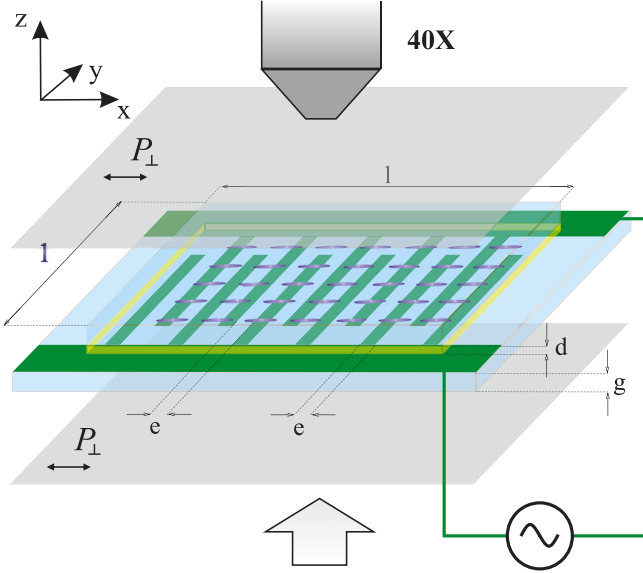


FIG. 1. (Color online) Sketch of the experimental setup, which represents an in-plane-switching cell connected to a generator and observed by a microscope (top), with  $40\times$  magnification, in white light (bottom). Thickness between the two glass plates,  $d = 8.8 \pm 0.2 \mu\text{m}$ . Thickness of a glass plate,  $g = 1 \text{ mm}$ . Active zone,  $l \times l = 1 \text{ cm}^2$ . Gap between two electrodes,  $e = 15 \mu\text{m}$ . Parallel polarizers to the molecules anchoring,  $P_{\perp}$  (following the  $x$  axis).

## II. ZIG-ZAG WALL LATTICE IN A IN-PLANE-SWITCHING NEMATIC LIQUID CRYSTAL CELL

### A. Experimental setup

The experimental configuration under study is depicted in Fig. 1. A layer of *E7* nematic liquid crystal is inserted between two glass plates (thickness  $g = 1 \text{ mm}$ ) with a cell gap  $d = 8.8 \pm 0.2 \mu\text{m}$ . The elastic constants of the liquid crystal are, respectively,  $K_1 = 11.2$ ,  $K_2 = 6.8$ , and  $K_3 = 18.6$  ( $\times 10^{-12} \text{ N}$ ). The parallel and the perpendicular dielectrical constants are  $\epsilon_{\parallel} = 18.96$  and  $\epsilon_{\perp} = 5.16$ , respectively [4,5]. We consider an in-plane-switching cell, with a homogeneous planar alignment (following the  $x$  axis, cf. Fig. 1) and a parallel rubbing to the electric field (Instec, IPS02A89uX90). The indium tin oxide electrode width and the gap width are the same,  $e = 15 \mu\text{m}$ . The height of the electrodes is negligible ( $\sim 25 \text{ nm}$ ) compared to the cell thickness ( $d = 8.8 \mu\text{m}$ ). The active zone is a square of side  $l = 1 \text{ cm}$ . Under these settings, we can consider the cell in a good approximation as an infinite system. The electrodes are connected to a function generator. An alternating current voltage is applied with frequencies  $\sim 10 \text{ Hz}$ – $100 \text{ kHz}$  and an amplitude  $\sim 10 \text{ V}_{\text{pp}}$ – $20 \text{ V}_{\text{pp}}$  (volt peak to peak). A white light illuminates the cell, which is placed between two parallel linear polarizers and observed with an optical microscope. The microscope magnification used is  $40\times$ . A charge-coupled-device (CCD) camera connected to a microscope allows us to record and measure the liquid crystal dynamics. We have increased the contrast of the experimental images to improve the visibility.

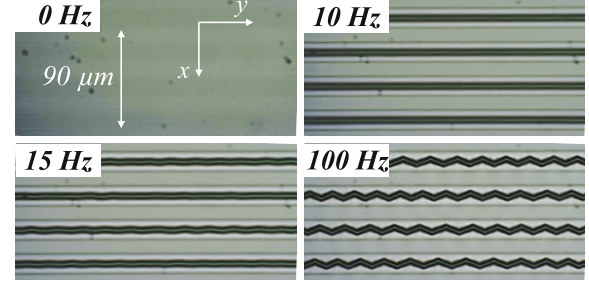


FIG. 2. (Color online) Wall lattice, experimental snapshots without voltage (top left panel) and for  $T = 20 \text{ V}_{\text{pp}}$  with different frequencies: top right panel,  $f = 10 \text{ Hz}$ , Ising wall lattice; bottom left panel,  $f = 15 \text{ Hz}$ , undulating wall lattice; bottom right panel,  $f = 100 \text{ Hz}$ , zig-zag wall lattice.

### B. Experimental observation of the wall lattices

Using the CCD camera, we can observe a small portion of the sample. By direct observations, without applying a voltage to the sample, one detects only the bands of electrodes. Figure 2 (top left) shows these bands of electrodes characterized by a darker gray zone. The gap between two consecutive electrodes and the size of the electrodes are the same,  $e = 15 \mu\text{m}$ . When applying voltage with an amplitude of  $20 \text{ V}_{\text{pp}}$ , with a low frequency,  $f = 10 \text{ Hz}$ , the system exhibits an Ising wall lattice, following the  $y$  axis (cf. top right panel of Fig. 2). This Ising wall lattice is a consequence of the transverse periodic electric field with an undulatory structure induced by the in-plane switching electrodes. Then the molecules are oriented according to the electric field since  $\epsilon_a = \epsilon_{\parallel} - \epsilon_{\perp} > 0$ . Figure 3 depicts the transverse structure of the electric field and the director orientations inside the sample. Hence, the Ising wall lattice is observed as a consequence of the molecular reorientation. This effect can be viewed with two parallel polarizers positioned parallel to the molecules anchoring. The white lines in the top right panel of Fig. 2 indicate that the molecules are vertical (following the  $z$  axis). In this case, the light can cross this region. The dark stripes represent a decrease of the light intensity crossing the second polarizer.

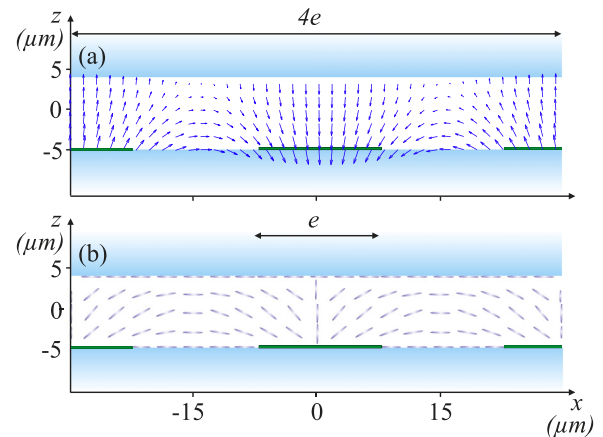


FIG. 3. (Color online) (a) The electric field representation inside the liquid crystal sample using formula (4). (b) The molecules orientation in the liquid crystal sample.

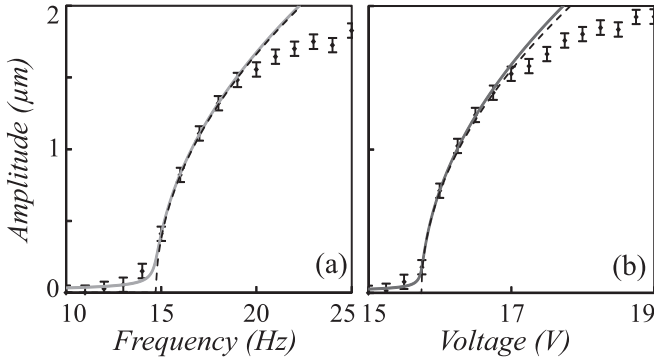


FIG. 4. Experimental characterization of the undulation wall. Amplitude of the undulation wall vs (a) frequency for  $V = 20 V_{pp}$ ; (b) amplitude for  $f = 100$  Hz.  $\blacklozenge$  experimental points; the dashed and solid lines, respectively, represent the analytical expectation value  $|a_{\max}|$  of Eq. (1) without and with noise, respectively. (a)  $\alpha = 0.53$ ,  $f_0 = 14.7$  Hz;  $\alpha = 0.53$ ,  $f_0 = 14.7$  Hz,  $\eta = 0.005$ . (b)  $\alpha' = 1.92$ ,  $V_0 = 15.7$  V;  $\alpha' = 2.02$ ,  $V_0 = 15.7$  V,  $\eta = 0.002$ .

This is due to the light polarization changing when it crosses the liquid crystal sample. The wavelength of this lattice is directly related to the electrodes size,  $\lambda_0 = 2e = 30 \mu\text{m}$ .

Increasing the frequency to  $f = 15$  Hz and maintaining the voltage, we observe the appearance of a supercritical modulational instability or spatial bifurcation following the  $x$  axis. At the onset of the modulational instability, the lattice is characterized by the presence of a fundamental mode (sinusoidal wall). We term this structure an *undulating wall lattice*. The typical undulating wall lattice is shown in the lower left panel of Fig. 2. The wavelength of the undulation depends slightly on the frequency and on the applied voltage, as it is depicted in the bottom panels of Fig. 4. This wavelength is typically of the order of  $28.5 \pm 0.5 \mu\text{m}$ . The amplitude of the undulation, as function of the voltage and the frequency, is presented in Figs. 4(a) and 4(b). From this figure, one concludes that the modulational bifurcation is of supercritical type, and close to the bifurcation the amplitude grows with a power law of the square root [cf. dashed curves in Figs. 4(a) and 4(b)]. Such an exponent is universal and is generically observed in the appearance of patterns in nonequilibrium systems [30–34]. Far from the bifurcation, the amplitude of the undulation moves away from this law due to the nonlinearities of the system. Below the bifurcation point, we observe experimentally a disordered and incoherent pattern, which is a result of a balance between fluctuations and dissipation. This phenomenon is well known as a precursor [35–37].

Recently, one of our authors has analytically characterized the universal shape of noisy bifurcation diagrams for the expectation value [36–38]. In the case of the supercritical bifurcation, it reads

$$|a_{\max}| = \sqrt{\frac{\varepsilon + \sqrt{\varepsilon^2 + 2\eta}}{2}}, \quad (1)$$

where  $\varepsilon$  and  $\eta$  are the bifurcation parameter and the noise level intensity, respectively. In our physical system, the control parameter is driven by the frequency or voltage. Fixing the voltage (frequency), the bifurcation parameter takes the form

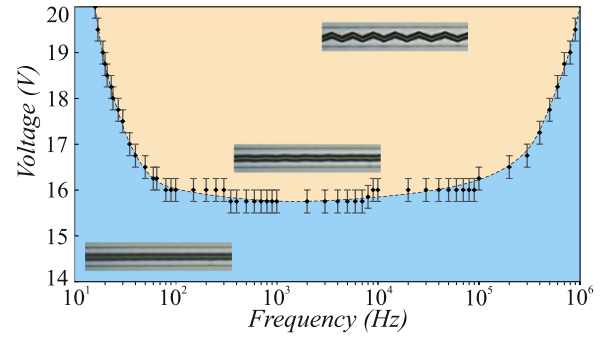


FIG. 5. (Color online) Phase diagram of the wall lattice in the frequency and voltage domain. The dark and the light zones account for the regions of Ising and zig-zag wall lattice, respectively. Dashed curve accounts for the modulational instability.  $\blacklozenge$  stands for experimental points of the spatial bifurcations.

$\varepsilon = \alpha[f - f_0]$ , where  $\alpha$  is a parameter of order 1 and is determined by other physical magnitudes, see Fig. 4(a) [for  $\varepsilon = \alpha'[V - V_0]$  see Fig. 4(b)]. Using the above expression, Eq. (1), as a fitting formula, we can determine the bifurcation point and the noise level intensity. We have a quite good agreement between the fits and the experimental data, as illustrated in Fig. 4. Dashed curves are obtained neglecting the effect of noise ( $\eta = 0$ ), which corresponds to the deterministic bifurcation diagram.

Increasing further the frequency, the undulation amplitude is bigger and the sinusoidal walls are replaced by a wall composed by straight segments with opposite slopes connected by a region of strong curvature giving rise to a wall with a zig-zag structure. Therefore, the system exhibits a *zig-zag wall lattice*. Figure 2, in the lower right panel, shows the typical observed zig-zag wall lattice. Note that by increasing the frequency or the voltage, the number of unstable spatial modes increases, and then the wall exhibits a more complex equilibrium. However, the walls amplitude has a saturation induced by the electrodes geometry.

We have experimentally characterized the phase diagram of the wall lattices in the space of frequency and voltage. Figure 5 illustrates the phase diagram. The frequency domain where we observe the zig-zag instability is between  $f = 15 \pm 1$  Hz and  $f = 1 \pm 0.1$  MHz, for the maximal accessible voltage value  $V_0 = 20 V_{pp}$ . Outside this domain, we have some capacitance effects, which do not allow us to observe the wall lattices. A minimal voltage threshold is observed in a large frequency band ( $f = 70$  Hz–90 kHz) for  $V_0 = 15.75 \pm 0.25 V_{pp}$ . Hence, for low voltages in a wide range of frequencies we only observe Ising wall lattices. Increasing the voltage, this lattice presents a spatial instability generating an undulating wall lattice, and at higher voltages it becomes zig-zag type. Therefore, as a function of frequency and voltage one can generate a *programmable wall lattice*, in which one can change the amplitude and the wavelength.

### C. Spatiotemporal evolution of Ising walls

To study spatiotemporal dynamics of the walls, we have identified the white line in the black strips (see Fig. 2), as the wall amplitude. Initially, we consider the sample at a low

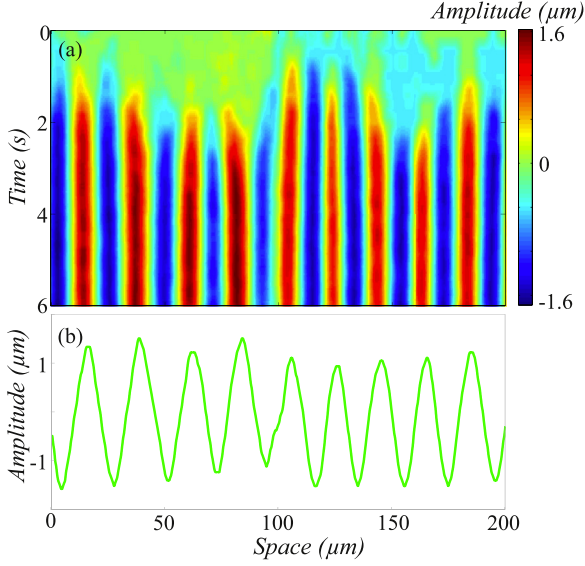


FIG. 6. (Color online) Spatiotemporal diagram (smoothed) of a Ising wall. (a) Experimental spatiotemporal of the pattern, and (b) plot of the last line of the spatiotemporal diagram.  $V = 17 V_{pp}$  and  $f = 1$  kHz.

voltage and a high frequency ( $f = 1$  kHz), then we abruptly increased the voltage to  $V = 17 V_{pp}$ . We record the temporal evolution of the Ising wall. Figure 6 shows the spatiotemporal diagram of the amplitude of a wall in the center of the sample. The spatial structure of the wall emerges in fewer than 2 s (cf. Fig. 6), with a well-defined periodicity. After 4 s, the dynamics is stationary. The smoothed pattern profile of the last state of the spatiotemporal diagram shows a zig-zag structure like those observed in similar experiments in liquid crystals [13,16,21]. However, in our case the pattern amplitude is limited by the electric field induced by the electrodes geometry.

### III. THEORETICAL DESCRIPTION OF THE ZIG-ZAG WALL LATTICE

To understand the origin of the wall lattice, first, we must characterize the electric field structure inside the nematic liquid crystal sample.

#### A. Voltage and electric field inside the nematic liquid crystal cell

The nematic liquid crystal is an anisotropic medium, so the voltage  $V(x, y, z)$  inside the cell satisfies an anisotropic Laplace equation, which has the form

$$\partial_{xx} V + \frac{\epsilon_{\perp}}{\epsilon_{\parallel}} \nabla_{\perp}^2 V = 0,$$

where  $\nabla_{\perp}^2$  is the Laplacian operator in the transversal coordinates to the unit vector  $\hat{x}$  and  $\epsilon_{\perp}$  and  $\epsilon_{\parallel}$  are, respectively, the perpendicular and the parallel dielectric constants to the nematic director. The dielectric anisotropy is defined as  $\epsilon_a \equiv \epsilon_{\parallel} - \epsilon_{\perp}$  and it is positive for the liquid crystal used in our experiment,  $\epsilon_a > 0$ . The voltage satisfies the boundary conditions  $V(x, y, -d/2) = f(x)$  and  $V(x, y, d/2) = 0$ , with  $f(x)$  a periodical function which follows the electrodes

periodicity. Using the Fourier transform in the  $x$  coordinate, neglecting the dependence on the  $y$  coordinate and solving the above equation with the corresponding boundary conditions, after straightforward calculations one obtains [39]

$$V(\vec{r}) = \int dk dx' \exp[-ik(x' - x)] f(x') \frac{\sinh[\Gamma k(\frac{d}{2} - z)]}{2\pi \sinh(\Gamma kd)}, \quad (2)$$

where  $k \equiv \pi/2e$ ,  $\Gamma \equiv \sqrt{\epsilon_{\perp}/\epsilon_{\parallel}}$ , and  $\exp[x]$  stands for the exponential function. For simplicity, we consider  $f(x) = V_0 \cos(kx)$ , where  $e$  is the electrode size and  $4e$  is the wavelength of the  $f(x)$  function. Thus the voltage inside the cell takes the form

$$V(x, y, z) = -V_0 \cos(kx) \frac{\sinh[\Gamma k(z - d/2)]}{\sinh(\Gamma kd)}, \quad (3)$$

then the voltage is a periodical function in the transverse direction and a decreasing function in the vertical direction. The electric field  $\mathbf{E} = -\nabla V$  inside the sample has the explicit form

$$\mathbf{E} = V_0 k \Gamma \cos(kx) \frac{\cosh[\Gamma k(z - d/2)]}{\sinh(\Gamma kd)} \hat{z} - V_0 k \sin(kx) \frac{\sinh[\Gamma k(z - d/2)]}{\sinh(\Gamma kd)} \hat{x}. \quad (4)$$

Figure 3(a) depicts the electric field in the liquid crystal sample. Since the liquid crystal has positive anisotropic constant  $\epsilon_a$ , the molecules align with the electric field. Figure 3(b) shows the expected structure for a director within the liquid crystal sample. Then the electric field induces naturally nematic Ising walls.

To understand the origin of the walls and their instabilities, first we will consider only the effect of the transverse electric field, which will allow us to understand the emergence of straight walls. Then we will consider the effect of the horizontal field together with the anisotropic features of the nematic liquid crystal that will be responsible of the zig-zag wall emergence.

#### B. Nematic Ising walls

The dynamical equation for the molecular director  $\mathbf{n}$ , reads [2–4]

$$\begin{aligned} \gamma \partial_t \mathbf{n} = & K_3 [\nabla^2 \mathbf{n} - \mathbf{n}(\mathbf{n} \cdot \nabla^2 \mathbf{n})] \\ & + (K_3 - K_1) [\mathbf{n}(\mathbf{n} \cdot \nabla)(\nabla \cdot \mathbf{n}) - \nabla(\nabla \cdot \mathbf{n})] \\ & + (K_2 - K_3) [2(\mathbf{n} \cdot \nabla \times \mathbf{n})(\mathbf{n}(\mathbf{n} \cdot \nabla \times \mathbf{n}) - \nabla \times \mathbf{n}) \\ & + \mathbf{n} \times \nabla(\mathbf{n} \cdot \nabla \times \mathbf{n})] + \epsilon_a (\mathbf{n} \cdot \mathbf{E})(\mathbf{E} - \mathbf{n}(\mathbf{n} \cdot \mathbf{E})), \end{aligned} \quad (5)$$

where  $\gamma$  is the rotational viscosity, and  $\{K_1, K_2, K_3\}$  are the elastic constants of the liquid crystal, which are related to splay, twist, and bend deformations, respectively [2–4].

To simplify, we will focus, in our theoretical description, on taking just one electrode and on considering that the transverse dimensions of the system are infinite. The base state for the molecules with an in-plane anchoring is  $\mathbf{n} = \hat{x}$ . It is equivalent to a state where the molecules are orthogonal to the electrode. Note that this state is a trivial equilibrium of Eq. (5). Considering only an electric field constant in the vertical direction,  $\mathbf{E} = E_z \hat{z}$ , it is easy to show the existence

of stable nematic Ising walls. Let us consider the following ansatz for the molecular director:

$$\mathbf{n}(x, y, z; t) = \begin{pmatrix} 1 - \frac{u^2}{2} \cos^2\left(\frac{\pi z}{d}\right) \\ 0 \\ u(x, y; t) \cos\left(\frac{\pi z}{d}\right) \end{pmatrix} + \mathbf{W}[u], \quad (6)$$

where  $u(x, y; t)$  accounts for the amplitude of the first Fourier mode in the  $z$  axis and  $\mathbf{W}[u]$  stand for higher nonlinear corrections in  $u$ . Introducing the above ansatz in Eq. (5), linearizing in  $\mathbf{W}[u]$  and imposing the solubility condition [13,31], one obtains

$$\gamma \partial_t u = \varepsilon u - bu^3 + (K_3 \partial_{xx} + K_2 \partial_{yy})u, \quad (7)$$

where  $\varepsilon \equiv \varepsilon_a E_z^2 - K_1 \pi^2 / d^2$  is a bifurcation parameter for the Fréedericksz transition and  $b \equiv 3/4((K_1 - K_3)\pi^2 / d^2 + \varepsilon_a E_z^2)$  stands for the nonlinear saturation. Close to the Fréedericksz transition [6],  $\varepsilon \ll 1$ , the above equation was derived using the amplitude  $u$  which is a slow variable in space and time and further considering the asymptotic limit  $u \sim \varepsilon^{1/2}$ ,  $\partial_y^2 \sim \partial_x^2 \sim \varepsilon$ ,  $\partial_t \sim \varepsilon$ ,  $K_1 \sim K_3 \sim 1$ ,  $K_2 \sim 1$ . For higher voltages than the Fréedericksz transition,  $\varepsilon > 0$ , the above model, Eq. (7), exhibits Ising wall solutions of the forms

$$u_{\perp}(x) = \pm \sqrt{\frac{\varepsilon}{b}} \tanh\left(\sqrt{\frac{\varepsilon}{2K_3}}(x - x_0)\right) \quad (8)$$

and

$$u_{\parallel}(y) = \pm \sqrt{\frac{\varepsilon}{b}} \tanh\left(\sqrt{\frac{\varepsilon}{2K_2}}(y - y_0)\right), \quad (9)$$

where  $u_{\perp}(x)$  and  $u_{\parallel}(y)$  are Ising walls parallel to the  $y$  axis and the  $x$  axis.  $x_0$  and  $y_0$  define the position of the walls. Hence, these solutions are parameterized by a continuous parameter that describes their position. Note that the only difference between these walls is the size of the wall core, which is determined by the respective elastic constants.

To study the stability of these walls we consider the following ansatz:

$$u(x, P(y, t)) = u_{\perp}[x - P(y, t)] + w(x, P), \quad (10)$$

which accounts for a disturbance of the wall in the transverse direction ( $x$  axis) and  $w$  describes the corrections due to the disturbance. Introducing the ansatz (10) in Eq. (7), linearizing in  $w$ , and imposing the solubility condition [31], one gets the diffusion equation

$$\gamma \partial_t P = K_2 \partial_{yy} P. \quad (11)$$

Therefore, perturbations of the wall are characterized by a diffusive dynamics and then the wall is stable. Analogously one can do the same analysis for the wall  $u_{\parallel}$  and conclude that it is also stable. In the next subsection, we will analyze the effect of considering a horizontal electric field.

### C. Derivation of the wall equation

Experimentally, the zig-zag instability of an Ising wall was observed for higher intensities of the electric field, far from the Fréedericksz transition, which is typically a few volts [4]. Thus, the previous analysis is no longer valid. Since the vertical component of the electric field is too strong, we can conjecture the emergence of two boundary layers touching

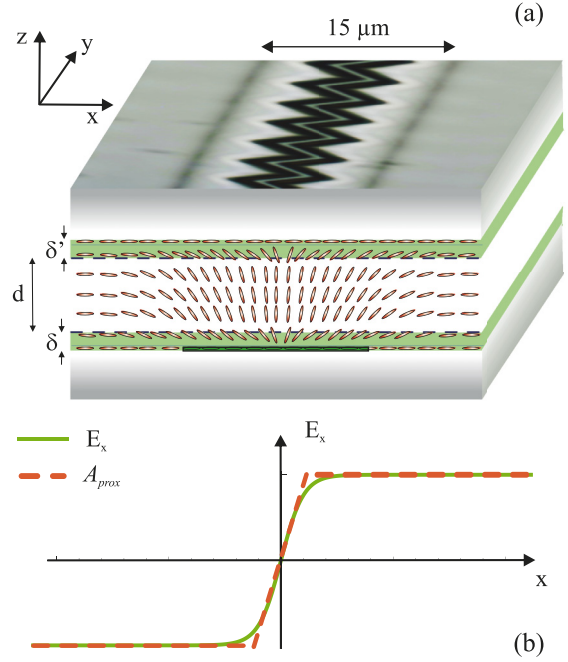


FIG. 7. (Color online) (a) Molecules orientation in the liquid crystal sample, showing the two boundary layers in green with a thickness  $\delta$  and the bulk in white with a thickness  $d$ . (b) Horizontal component of the electric field representation (continuous line) and its approximation (dashed curve).

the glass layers, where the molecules reorient in a complex manner under the anchoring boundary conditions, whereas in the bulk the molecules are mainly oriented perpendicularly to the glasses ( $\mathbf{n} = \hat{\mathbf{z}}$ ) (cf. Fig. 7). The thickness of these boundary layers is characterized by the parameter  $\delta$ . The above description is valid over the electrode area, where the vertical component of the electric field,  $E_z$ , is the highest. The molecules above the gap area are mainly oriented in the  $x$  axis, where the horizontal electric field  $E_x$  is more important than  $E_z$  (see Fig. 7). Therefore, at a high electric field intensity, we can consider an effective homeotropic anchoring medium in the bulk of the sample, neglecting the boundary condition occurring in the boundary layer. Hence, in order to describe the dynamics of the interface we can consider the following ansatz for the molecular director  $\mathbf{n}$  in the bulk:

$$\mathbf{n} = \begin{pmatrix} u \cos(\pi z/d) \\ \frac{K_1}{a} \partial_{xy} u \cos\left(\frac{\pi z}{d}\right) + \frac{K_1^2}{a^2} \partial_{xy^3} u \cos^2\left(\frac{\pi z}{d}\right) \\ 1 - \frac{u^2}{2} \cos^2(\pi z/d) \end{pmatrix} + \mathbf{W}[u], \quad (12)$$

where  $u(x, y; t)$  accounts for the amplitude of the first Fourier mode in the  $x$  component and  $\mathbf{W}[u]$  stands for higher nonlinear corrections in  $u$  and  $a \equiv \varepsilon_a E_z^2 + K_3 \pi^2 / d^2$ . Note that when  $u = 0$ , the system exhibits, as an equilibrium, a homeotropic state in the bulk, i.e., the molecules are oriented perpendicularly to the glass plates. Considering an electric field of the form  $\mathbf{E} = E_z \hat{\mathbf{z}} + E_x \hat{\mathbf{x}}$ , introducing the above ansatz, expression (12), in Eq. (5), linearizing in  $\mathbf{W}[u]$  and imposing

the solubility condition [13,31], one obtains

$$\begin{aligned} \gamma \partial_t u &= \tilde{\varepsilon} u - \tilde{b} u^3 + K_1 \partial_{xx} u \\ &+ K_2 \partial_{yy}^2 + \frac{K_1^2}{a} \partial_{x^2 y^2} u + \frac{K_1^3}{a^2} \partial_{x^2 y^4} u - \frac{3}{4} K_3 u (\partial_y u)^2 \\ &+ \frac{2}{d} \epsilon_a E_z E_x, \end{aligned} \quad (13)$$

where  $\tilde{\varepsilon} \equiv -\epsilon_a E_z^2 - K_3 \pi^2 / d^2 + \epsilon_a E_x^2$  is a bifurcation parameter for the effective Fréedericksz transition of the bulk homeotropic media and  $\tilde{b} \equiv (K_1 - 3K_3/2)\pi^2/2d^2 - 3\epsilon_a E_z^2/4$  is a saturation parameter. The above equation was derived using the fact that the amplitude  $u$  is a slowly variable in space and time and further by considering the asymptotic limit  $u \sim \varepsilon^{1/2}$ ,  $\partial_t \sim \varepsilon$ ,  $\partial_y^2 \sim \mu$ ,  $\partial_x^2 \sim \varepsilon$ ,  $K_1 \sim K_3 \sim 1$ ,  $K_2 \sim \varepsilon$ ,  $E_z \sim 1$ ,  $E_x \sim \varepsilon$ ,  $\mu \equiv (K_2/\varepsilon - 2K_1/5a)$ , and  $\varepsilon \ll \mu \ll 1$ . Note that the horizontal component of the electric field has the form illustrated in Fig. 7(b). To achieve simpler calculations we approach this function by straight lines [cf. to the dotted lines in Fig. 7(b)]. Thus near the electrode  $E_x(x) \approx -(\Delta E/e)x \sim \mu$ .

Then, in the previous asymptotic limit, the first three terms of the right side of Eq. (13) are dominant and all other terms are corrective. The dominate equation only has  $u_\perp(x - x_0)$  as Ising walls. In order to understand the effect of the perturbative terms, we consider the following ansatz:

$$u(x, t) = u_\perp[x - P(y, t)] + w(x, P), \quad (14)$$

where  $u_\perp$  is considering  $\{\varepsilon, b, K_3\}$  by  $\{\tilde{\varepsilon}, \tilde{b}, K_1\}$ ,  $P(y, t)$  is a field that accounts for the position and the dynamic of the wall. Introducing this ansatz in Eq. (13) and linearizing in  $w$ , we obtain

$$\begin{aligned} \mathcal{L}w &= \gamma \partial_t P (\partial_x u_\perp) - K_2 P_{yy} (\partial_x u_\perp) + P_y^2 (\partial_x^2 u_\perp) \\ &+ \frac{K_1 \varepsilon}{2a} [-P_{yy} (\partial_x^3 u_\perp) + P_y^2 (\partial_x^4 u_\perp)] \\ &+ \frac{K_1^2 \varepsilon}{2a^2} [-P_{yyyy} (\partial_x^3 u_\perp) + 4P_y P_{yyy} (\partial_x^4 u_\perp) \\ &+ 3P_{yy}^2 (\partial_x^4 u_\perp) - 6P_y^2 P_{yy} (\partial_x^5 u_\perp) + P_y^4 (\partial_x^6 u_\perp)] \\ &- \frac{3}{4} K_3 P_y^2 u_\perp (\partial_x u_\perp)^2 - q(x + P), \end{aligned} \quad (15)$$

with  $q = 2\epsilon_a E_z \Delta E \sqrt{2K_1/\varepsilon}/de$  and the linear operator  $\mathcal{L} = -(\varepsilon - 3bu_0^2 + K_1 \partial_x^2)$ . This operator is a Hermitian one with respect to the inner product  $\langle f|g \rangle = \int_{-\infty}^{+\infty} fg dx$ ,  $\mathcal{L} = \mathcal{L}^\dagger$ . As consequence of the translation invariance of the dominate part of Eq. (13), this operator has a Goldstone mode, that is,  $\mathcal{L}^\dagger \partial_{x_0} u_0 = 0$ . To solve the above linear equation, we use the Fredholm alternative or solubility condition [31], i.e., the right side of Eq. (15) is orthogonal to the kernel of  $\mathcal{L}^\dagger$ . Note that because  $u_\perp$  is an odd function the scalar products  $\langle \partial_x u_\perp | \partial_x^2 u_\perp \rangle$ ,  $\langle \partial_x u_\perp | \partial_x^4 u_\perp \rangle$ ,  $\langle \partial_x u_\perp | \partial_x^6 u_\perp \rangle$ ,  $\langle \partial_x u_\perp | u_\perp (\partial_x u_\perp)^2 \rangle$ , and  $\langle \partial_x u_\perp | x \rangle$  vanish. Hence, the previous solubility conditions leads to the *wall equation*,

$$\gamma \partial_t P = D_1 P_{yy} + D_2 P_y^2 P_{yy} - D_3 P_{yyyy} - 2qP,$$

where  $D_1 = K_2 - 2K_1 \varepsilon / 5a$ ,  $D_2 = 48K_1^2 \varepsilon / 7a^2$ , and  $D_3 = 2K_1^2 \varepsilon / 5a^2$ . Rescaling space, time, and field in the following manner:  $t' \equiv t/\gamma$ ,  $y' \equiv y/\sqrt{D_3}$ , and  $P' = P/\sqrt{D_3/D_2}$ , the

asymptotic equation for  $P$  leads to (omitting the apostrophes)

$$\partial_t P = DP_{yy} + P_y^2 P_{yy} - P_{yyyy} - \lambda P, \quad (16)$$

where  $D \equiv D_1/\sqrt{D_3} = (K_2 - 2K_1 \varepsilon / 5a)/\sqrt{2K_1^2 \varepsilon / 5a^2}$  and  $\lambda = 8\epsilon_a E_z \Delta E \sqrt{2K_1/\varepsilon}/de$ . The above wall model is a nonlinear diffusion equation with a linear relaxation, where the coefficient  $D$  accounts for the diffusion, the second and the third terms stand for the nonlinear diffusion and the hyperdiffusion, and the last term reports for the linear relaxation. When  $\lambda$  is zero this model has been widely used to describe the dynamics of interfaces between symmetric states [13]. In this case, if one introduces the variable change  $\Lambda \equiv \partial_x P$ , Eq. (16) becomes the Cahn-Hilliard equation [40,41]. This model describes the dynamics of phase separation in conservative systems. The introduction of  $\lambda$  modifies this model to a modified Cahn-Hilliard equation.

#### D. Zig-zag instability of a wall

The wall dynamics is described by Eq. (16). When  $D$  is positive, i.e., for low voltages, the above model describes a diffusion equation with a linear relaxation. Then  $P = 0$  is a stable solution, that is, the straight wall located on the electrode is stable. The above scenario changes while increasing the voltage, the sign of the diffusion coefficient changes and the wall becomes unstable. To study this dynamics, we perform a linear stability analysis. Using  $P = P_0 \exp[-ikx + \sigma t]$ , where  $P_0$  is a constant in Eq. (16), after straightforward calculations we obtain the growth rate relation

$$\sigma(k) = -Dk^2 - k^4 - \lambda. \quad (17)$$

Figure 8 shows the above relationship for different values of the relaxation parameter. The instability condition is obtained when this growth rate curve crosses the horizontal axis. The most unstable mode corresponds to the maximum of  $\sigma(k)$ , which occurs in  $k_c^2 = -D/2$ . The instability condition  $\sigma(k_c) = 0$ , allows us to find the critical relation  $\lambda_c = D^2/4$  [cf. Fig. 8(a)]. In Fig. 8, the wall is shown below and above the spatial instability. The numerical simulations show a quite good qualitative agreement with experimental observations of wall lattice, see Figs. 8(b)–8(d). Hence, this wall equation (16) is an appropriate model to describe the dynamics of a wall. Figure 9 outlines the spatiotemporal evolution of the wall when it suffers from the spatial instability. We note that the experimental system exhibits a similar dynamical behavior (cf. Fig. 6).

#### E. Undulating wall

To study the dynamics of the wall close to the spatial instability, we will perform weakly nonlinear analysis. Let us consider the bifurcation parameter near the instability,  $\lambda = \lambda_c - \Delta$ , and introducing the ansatz for  $P$ ,

$$P(y, t) = A(y, t) \exp[ik_c y] + A^* \exp[-ik_c y] + w, \quad (18)$$

where  $A(y, t)$  accounts for the amplitude of the critical spatial mode, we assume that close to the bifurcation this amplitude is a slow variable in time and space, and  $w$  stands for nonlinear corrections. Replacing this ansatz, expression (18) in Eq. (16), linearizing in  $w$ , and imposing the solubility conditions, we get

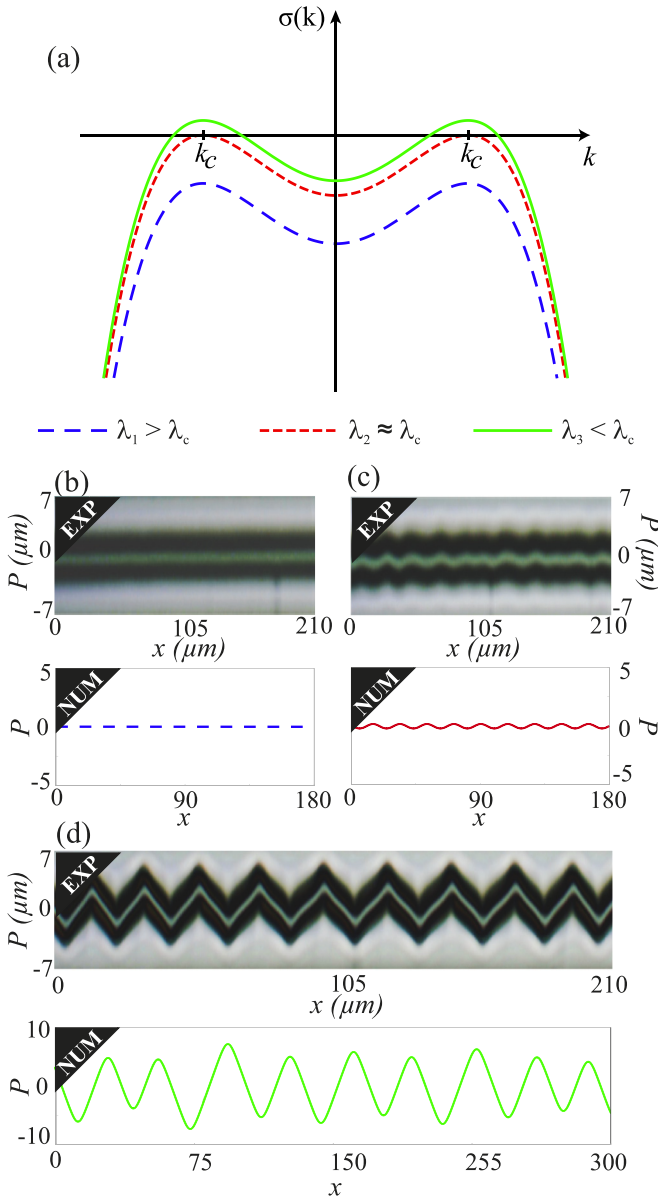


FIG. 8. (Color online) Interface dynamics. (a) Growth rate relation, Eq. (17), for three values of  $\lambda$ . Experimental and numerical interface profiles for the three previous cases: (a)  $f = 10$  Hz (exp),  $\lambda_1 = 0.30$  (num); (b)  $f = 15$  Hz (exp),  $\lambda_1 = 0.24$  (num); (c)  $f = 100$  Hz (exp),  $\lambda_1 = 0.0001$  (num).  $V = 20 V_{pp}$  (exp),  $D = -1$  (num),  $\lambda_c = D^2/4 = 0.25$ .

the Ginzburg-Landau equation with real coefficients [31,32],

$$\partial_t A = \Delta A - \frac{D^2}{4} A |A|^2. \quad (19)$$

This is a universal model describing pattern formation in a supercritical spatial bifurcation [31,32]. Using a polar representation,  $A = R e^{i\phi}$ , the above equation reads

$$\begin{aligned} \dot{\phi} &= 0, \\ \dot{R} &= \Delta R - \frac{D^2}{4} R^3, \end{aligned} \quad (20)$$

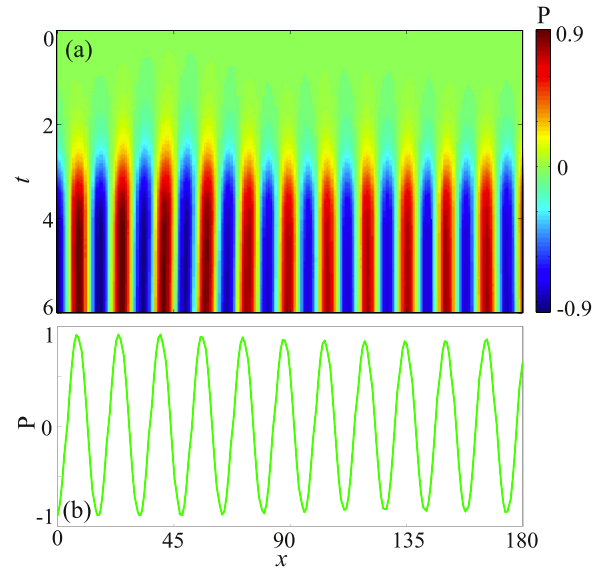


FIG. 9. (Color online) Spatiotemporal diagram of an Ising wall obtained from numerical simulations of the wall equation (16),  $D = -1$  and  $\lambda = 0.2$ . (a) Spatiotemporal evolution of the wall; (b) plot of the last line of the spatiotemporal diagram.

Then the trivial solution of this set of equations is that the phase  $\phi$  is an arbitrary constant; the modulus is constant and it is determined by the bifurcation parameter. In the case of  $\Delta < 0$ , the magnitude of the amplitude satisfies  $R = 0$  and  $\Delta \geq 0$ ,

$$R^* = \frac{2}{D} \sqrt{\Delta} = \frac{2}{D} \sqrt{\frac{D^2}{4} - \lambda}. \quad (21)$$

Then as a function of the bifurcation parameter the magnitude of the amplitude grows with the square root of it. Figure 10 shows the amplitude of the wall, model (16), as a function of the bifurcation parameter and compares it with the previous prediction, finding a quite good agreement close to the bifurcation. Note that experimentally we found a similar bifurcation diagram (see Fig. 4).

The present analysis of this section allows us to understand the dynamics of a zig-zag wall. Analogously, we can perform

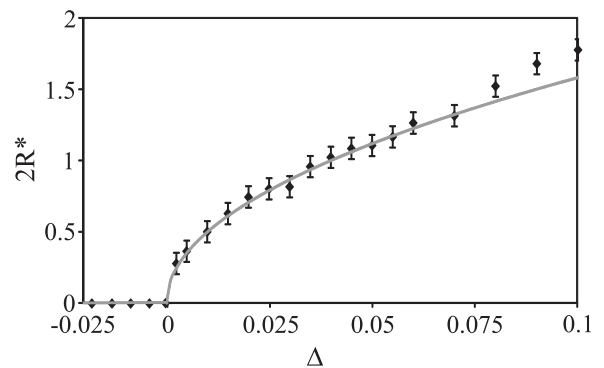


FIG. 10. Bifurcation diagram of the amplitude of the wall, model (16), as a function of the bifurcation parameter  $\Delta = D^2/4 - \lambda$ . The points represent the results obtained by numerical simulations of the model (16). The solid curve is obtained by using the formula (21).

this analysis for each Ising wall and then describe the emergence of the Ising wall lattice, the undulating wall lattice, and the zig-zag wall lattice

#### IV. CONCLUSIONS

In the present work, we have evidenced the observation of a programmable zig-zag lattice in a nematic liquid crystal inserted into an in-plane-switching cell. Applying a small voltage in a wide range of blue frequencies, the system exhibits an Ising wall lattice. By increasing the voltage, this lattice presents a spatial supercritical instability generating an undulating lattice, and at higher voltages this wall lattice becomes a zig-zag type. Experimentally, we have characterized the bifurcations and phase diagram of the wall lattice. Theoretically, we have developed, from first principles, a model to describe the dynamical behaviors of the walls. The dynamical behavior of each wall is described by a nonlinear diffusion equation

with a relaxation term, which we have termed wall equation. This model is equivalent to the Cahn-Hilliard equation with a relaxation term. The wall equation has a good qualitative agreement with the experimental observations.

This type of programmable wall lattice can be useful to have a deformable diffraction grating, which can offer new methods in images treatment. Works in this direction are in progress. The possibility of having electrodes with varied geometries may allow the creation of complex wall lattices, with new disordered behaviors such as a programmable lattice.

#### ACKNOWLEDGMENTS

The authors thank N. Maalouli for fruitful discussions. The authors acknowledge the financial support by ANR-CONICYT 39 (Grant No. ANR-2010-INTB-402-02), “Colors.” M.G.C. and V.O. acknowledge the financial support of FONDECYT Projects No. 1120320 and No. 3130382.

- 
- [1] M. G. Friedel, *Ann. Phys.* **18**, 273 (1922).
  - [2] P. G. de Gennes and J. Prost, *The Physics of Liquid Crystals*, 2nd ed. (Clarendon Press, Oxford, 1993).
  - [3] S. Chandrasekhar, *Liquid Crystal* (Cambridge University Press, New York, 1992).
  - [4] P. Oswald and P. Pieranski, *Nematic and Cholesteric Liquid Crystals* (Taylor & Francis, Boca Raton, FL, 2005).
  - [5] I. C. Khoo, *Liquid Crystals*, 2nd ed. (John Wiley & Sons, New York, 2007).
  - [6] V. Fréedericksz and V. Zolina, *Trans. Farad. Soc.* **29**, 919 (1933).
  - [7] W. Helfrich, *Phys. Rev. Lett.* **21**, 1518 (1968).
  - [8] F. Brochard, *J. Phys. (Paris)* **33**, 607 (1972).
  - [9] A. Hubert and R. Schafer, *Magnetic Domains* (Springer-Verlag, Berlin, 1998).
  - [10] L. N. Bulaevskii and V. L. Ginzburg, *Zh. Eksp. Teor. Fiz.* **45**, 772 (1963) [*Sov. Phys. JETP* **18**, 530 (1964)].
  - [11] P. Coulet, J. Lega, B. Houchmanzadeh, and J. Lajzerowicz, *Phys. Rev. Lett.* **65**, 1352 (1990).
  - [12] J. M. Gilli, M. Morabito, and T. Frisch, *J. Phys. II (France)* **4**, 319 (1994).
  - [13] C. Chevillard, M. Clerc, P. Coulet, and J.-M. Gilli, *Eur. Phys. J. E* **1**, 179 (2000); *Europhys. Lett.* **58**, 686 (2002).
  - [14] C. Chevillard and M. G. Clerc, *Phys. Rev. E* **65**, 011708 (2001).
  - [15] T. Nagaya and J. M. Gilli, *Phys. Rev. E* **65**, 051708 (2002); *Phys. Rev. Lett.* **92**, 145504 (2004).
  - [16] T. Ohzono and J. Fukuda, *Nat. Commun.* **3**, 701 (2012).
  - [17] Yu. A. Astrov, E. Ammelt, and H. G. Purwins, *Phys. Rev. Lett.* **78**, 3129 (1997).
  - [18] A. A. Golovin, S. H. Davis, and A. A. Nepomnyashchy, *Physica D* **122**, 202 (1998).
  - [19] R. Ragnarsson, J. L. Ford, C. D. Santangelo, and E. Bodenschatz, *Phys. Rev. Lett.* **76**, 3456 (1996).
  - [20] L. Limat, *Europhys. Lett.* **44**, 205 (1998).
  - [21] A. Dequidt and P. Oswald, *Eur. Phys. J. E. Soft Matter* **19**, 489 (2006).
  - [22] D. K. Yoon, J. Yoon, Y. H. Kim, M. C. Choi, J. Kim, O. Sakata, S. Kimura, M. W. Kim, I. I. Smalyukh, N. A. Clark, M. Ree, and H. T. Jung, *Phys. Rev. E* **82**, 041705 (2010).
  - [23] S. J. Woltman, G. D. Jay, and G. P. Crawford, *Liquid Crystals: Frontiers in Biomedical Applications* (World Scientific, Singapore, 2007).
  - [24] R. J. Bushby, S. M. Kelly, and M. O’Neill, *Liquid Crystalline Semiconductors*, Springer Series in Materials Science, Vol. 169 (Springer-Verlag, Berlin, 2013).
  - [25] R. H. Chen, *Liquid Crystal Displays: Fundamental Physics and Technology* (John Wiley & Sons, New York, 2011).
  - [26] J. Chen, W. Cranton, and M. Fihn, *Handbook of Visual Display Technology* (Springer, Berlin, 2012).
  - [27] R. A. Soref, *J. Appl. Phys.* **45**, 5466 (1974).
  - [28] R. Kiefer, B. Weber, F. Windscheid, and G. Baur, *Jpn. Displays* **92**, 547 (1992).
  - [29] M. Oh-e and K. Kondo, *Appl. Phys. Lett.* **67**, 3895 (1995).
  - [30] G. Nicolis and I. Prigogine, *Self-Organization in Non Equilibrium Systems* (J. Wiley & Sons, New York, 1977).
  - [31] L. M. Pismen *Patterns and Interfaces in Dissipative Dynamics*, Springer Series in Synergetics (Springer, Berlin, 2006).
  - [32] M. C. Cross and P. C. Hohenberg, *Rev. Mod. Phys.* **65**, 851 (1993).
  - [33] M. Cross and H. Greenside, *Pattern Formation and Dynamics in Nonequilibrium Systems* (Cambridge University Press, New York, 2009).
  - [34] L. Landau, *C. R. Acad. Sci. USSR* **44**, 311 (1944).
  - [35] W. Schöpf and W. Zimmermann, *Phys. Rev. E* **47**, 1739 (1993).
  - [36] G. Agez, M. G. Clerc, and E. Louvergneaux, *Phys. Rev. E* **77**, 026218 (2008).
  - [37] G. Agez, M. G. Clerc, E. Louvergneaux, and R. G. Rojas, *Phys. Rev. E* **87**, 042919 (2013).
  - [38] I. Ortega, M. G. Clerc, C. Falcon, and N. Mujica, *Phys. Rev. E* **81**, 046208 (2010).
  - [39] R. Barboza, U. Bortolozzo, G. Assanto, E. Vidal-Henriquez, M. G. Clerc, and S. Residori, *Phys. Rev. Lett.* **111**, 093902 (2013).
  - [40] J. W. Cahn and J. E. Hilliard, *J. Chem. Phys.* **28**, 258 (1958).
  - [41] H. Calisto, M. G. Clerc, R. Rojas, and E. Tirapegui, *Phys. Rev. Lett.* **85**, 3805 (2000).